

Context Cameras for the Orbiting Carbon Observatory 3 (OCO-3) Instrument

Colin McKinney, Timothy Goodsall, Michael Hoenk, Jacob Shelton, Keith Rumney, Christophe Basset, Muthu Jeganathan, and Douglas Moore

Jet Propulsion Laboratory, California Institute of Technology, 4800 Oak Grove Dr., Pasadena, CA 91109

Colin.McKinney@jpl.nasa.gov, Timothy.Goodsall@jpl.nasa.gov, Michael.E.Hoenk@jpl.nasa.gov,
Jacob.Shelton@jpl.nasa.gov, Keith.Rumney@jpl.nasa.gov, Christophe.Basset@jpl.nasa.gov,
Muthu.Jeganathan@jpl.nasa.gov, Douglas.M.Moore@jpl.nasa.gov

Abstract—We have developed an adaptable camera platform that takes advantage of screened and qualified commercial off the shelf (COTS) components (CMOS sensor, rad-tolerant microcircuits, lenses) to significantly shorten development time of space-borne visible imaging systems while reducing the overall cost and risk of the development. This modular camera platform is implemented as a suite of two visible-light cameras for the Orbiting Carbon Observatory 3 (OCO-3) instrument at NASA’s Jet Propulsion Laboratory (JPL). The Internal Context Camera (ICC) and External Context Camera (ECC) provide contextual engineering imaging support for the calibration of the OCO-3 instrument, intended to significantly reduce the duration of the mission’s calibration campaign.

The OCO-3 mission has taken advantage of the design and qualification work performed by JPL’s Mars 2020 Enhanced Engineering Camera (EECam) team in reusing the qualified COTS CMOS imaging sensor, proven electronic designs, and scalable field-programmable gate array (FPGA) firmware to meet OCO-3’s mission requirements and resource availability.

We will be presenting the steps taken by JPL to design, build, and test the Context Cameras for the OCO-3 mission. We will highlight the design deviations from the Mars2020 EECams and discuss the methodology of tailoring the EECam design for the OCO-3 requirements. Camera imaging capabilities, including focal plane and optical performance, will be presented, as well as a summary of the calibration and environmental test results. Finally, we will discuss the potential for future applications for the Context Cameras.

TABLE OF CONTENTS

1. INTRODUCTION	1
2. CAMERA SYSTEM OVERVIEW	1
3. OPTICS	2
4. DETECTOR	3
5. ELECTRONICS DESIGN	4
6. FPGA DESIGN	5
7. MECHANICAL DESIGN.....	7
8. CAMERA TESTING AND CALIBRATION.....	8
9. POTENTIAL FOR FUTURE USE	13
10. SUMMARY	14
ACKNOWLEDGEMENTS	14
REFERENCES.....	14
BIOGRAPHY	14

1. This work was carried out at the Jet Propulsion Laboratory, California Institute of Technology, under a contract with the National Aeronautics and Space Administration.

2. 978-1-5386-2014-4/18/\$31.00 ©2018 IEEE

1. INTRODUCTION

The Orbiting Carbon Observatory 3 (OCO-3) mission will monitor CO₂ levels from the International Space Station. The OCO-3 instrument includes two high-resolution context cameras in order to provide contextual imagery used in calibrating the instrument. While the context cameras enhance OCO-3 science performance by enabling faster calibration, they are not essential to meeting the OCO-3 science requirements. For this reason, the context cameras are designated ‘Class D’ mission-risk instruments, and take advantage of the use commercial, off-the-shelf (COTS) components (lenses and detector).

2. CAMERA SYSTEM OVERVIEW

The context cameras interface to the OCO-3 Payload Bus Electronics (PBE) for data and power. The context cameras receive +28V DC power from the instrument’s Power Conditioning Electronics (PCE), within the PBE. The Central Electronics Unit (CEU) within the PBE passes commands to and retrieves streaming imagery data from the context cameras using an LVDS interface.

The Internal Context Camera (ICC) provides data for alignment and calibration of the instrument’s telescope. The ICC is co-boresighted with the telescope, achieved with the use of a small pickoff mirror, as shown in Figure 1. The ICC optical performance is designed to provide monochromatic, visible-band images with a field of view and resolution comparable to the OCO-3 science channels [1].

To complement the ICC, the External Context Camera (ECC) provides color images covering a wider field of view, providing contextual pointing information of the instrument relative to the Earth’s surface. The ECC is located on the Pointing Mirror Assembly (PMA), external to the optical path of the instrument, as shown in Figure 2.

The two Context Cameras are identical apart from their lenses and choice of monochrome vs. color detector. Each camera consists of three compact electronic boards, a high-resolution image sensor, a radiation-tolerant FPGA, custom chassis, and a ruggedized COTS lens. See Table 1 for the OCO-3 context camera suite imaging performance.

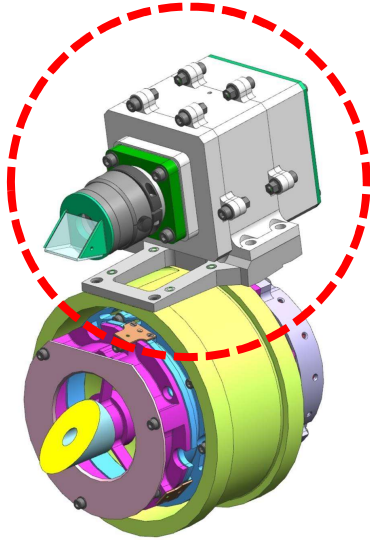


Figure 1. Internal Context Camera (ICC), mounted on telescope and co-boresighted with the instrument

Table 1. Context Camera Capabilities

Imaging Array Size	4480 x 3839 pixels
Pixel Size	$6.4\mu\text{m}^2$
Pixel Full Well	13k e-
Pixel Bit Depth	12 bits
Shutter	Global
ICC Optics	$32^\circ \times 28^\circ$ (H x V), f/5, iFOV < 0.125mrad/pixel
ECC Optics	$56^\circ \times 48^\circ$ (H x V), f/5, iFOV < 0.22mrad/pixel
Power	< 5W @ +28V input
Mass	ICC: 460g, ECC: 633g
Volume	ICC: 61mm x 63mm x 120mm ECC: 61mm x 63mm x 155mm

3. OPTICS

In order to minimize costs and reduce development schedule, the OCO-3 project baselined commercial lenses for the Context Cameras. The modest imaging requirements are such that a custom development was deemed unnecessary, and could be met with readily-available commercial options. The lenses are fixed-focus, fixed- focal length, fixed-aperture, and contain no moving parts, reducing the complexity of the optics and supporting camera electronics.

Imaging requirements fulfillment

The ICC uses a narrow-angle $32^\circ \times 28^\circ$ (H x V), f/5 C-Mount COTS lens. The ECC uses a medium-angle $56^\circ \times 48^\circ$ (H x V), f/5 V-mount COTS lens.

The large format detector used by the Context Cameras offered benefits to the lens selection for each camera type. In the case of the ECC, the full-frame color 20M pixel array

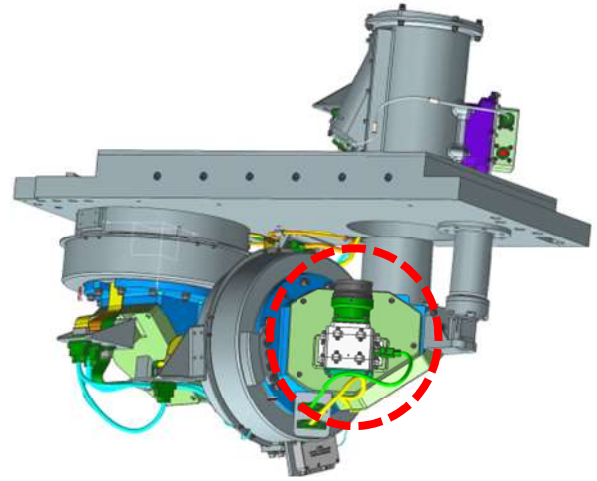


Figure 2. External Context Camera (ECC), mounted on the pointing mirror assembly elevation housing and co-boresighted with the instrument (red circle).

offers a large field of view and acceptable ground sampling distance (GSD) for the coarse contextual calibration of the instrument. For the ICC, the fine spatial sampling of the detector allowed the imaging requirements to be met without the need to fully fill the detector's active area. Therefore, the imaging circle of the ICC is smaller than the active area of the detector, but still subtends sufficient pixels to meet field of view and GSD requirements. This resulted in the selection of a smaller, less massive lens, saving instrument resources.

The Signal-to-Noise Ratio (SNR) requirement drove the sizing of each lens' aperture. In the case of these COTS lenses, it meant the adjustable iris was to be fixed to set the appropriate F-number ($1/f$) for each lens type. The internal and external context camera images are required to achieve an $\text{SNR} > 100:1$ for image pixels in which the signal level exceeds 70% of the detector's full well capacity, and at viewing angles of 60° off nadir and solar zenith angles $< 75^\circ$. As the detector contribution to satisfying the SNR requirement was fixed (capability driven), the aperture sizes were calculated analytically using radiometric modeling. For each lens, the aperture was set to f/5 such that the camera met SNR requirements while ensuring the detector pixels did not saturate under high-albedo conditions.

Lens ruggedization and qualification testing

Care was taken to ensure the lens housings could withstand the environments expected during the mission: thermal excursions and vibration levels. The COTS lenses were selected primarily to meet imaging requirements, with packaging and reliability a close secondary concern. To enhance reliability, the lenses were ruggedized in two ways – the adjustable iris was replaced with a fixed aperture, and the focus ring was locked at infinity. This work was performed by the lens vendor and verified upon receipt at JPL.

The lenses underwent environmental testing at JPL for thermal vacuum temperature and vibration levels, and imaging performance was verified post-environmental testing. The lenses were exposed to three thermal vacuum cycles from -40°C to +70°C. Additionally, the lenses saw vibration testing in three axes, as captured in Table 2.

Table 2. COTS Lens vibration levels

Frequency, Hz	Qual/Protoflight PF Level
20	0.032 g ² /Hz
20 - 50	+6 dB/octave
50 - 300	0.2 g ² /Hz
300 - 2000	-6.0 dB/octave
2000	0.0046 g ² /Hz
Overall	10.2 grms

The modular transfer function (MTF) of each lens was compared pre- and post-testing and exhibited no change.

4. DETECTOR

The high-resolution imaging capabilities of the context cameras is a result of the CMV20000 detector performance [2]. These are 20 megapixel, global shutter, CMOS imaging detectors manufactured by AMS Sensors Belgium (formerly CMOSIS). The detector is a monolithic CMOS ASIC comprised of a 5120x3840 array of 6.4µm x 6.4µm active pixels, analog signal chain, and digital signal processing circuits. The detector outputs 12-bit pixel depth imagery and requires only three low-voltage power supplies, serial digital interface, and a single input clock, allowing the supporting camera circuit design to be simple and straightforward.

The development of the context cameras was contingent on the use of the CMV20000 detectors, as significant non-recurring engineering and screening had to be performed to date within JPL. The camera's imaging capabilities are derived from the detector performance and the resultant detector testing sought to verify and validate advertised detector capabilities.

Imaging Performance

The CMV20000 is a front-illuminated detector with integrated microlenses. The ICC uses a monochrome detector to optimize for broadband visible response. The ECC uses a color detector, which adds Red, Green, and Blue (RGB) color filters beneath the microlenses. The color filters are arranged in the standard 2x2 Bayer pattern, with one red pixel, two green pixels, and one blue pixel.

The specified pixel full-well depth is small (15k e-) compared to astronomy-grade charge-coupled device (CCD) imagers (100k+ e-). However, the low read noise and dark current of the CMOSIS detector makes it suitable for high-flux scenes such as earth surface imaging for OCO-3, allowing the SNR

requirement to be met without the need to cool the detector. Pixel response non-uniformity (PRNU) and linearity were tested at the camera level of assembly and were found to match advertised performance.

COTS Detector Screening

JPL's Mars2020 rover commissioned new enhanced engineering cameras (EECAMs) to replace the highly successful MER/MSL Engineering Cameras (ECAM) [3]. To keep development costs low and meet demanding schedule constraints, a COTS CMOS detector was baselined, with the caveat that JPL use flight mission-assurance practices to qualify and screen the devices to assess suitability for mission-critical hardware. OCO-3 sought to leverage this screening and baselined the CMV20000 detector for their Context Cameras.

JPL's screening criterion is a tailored subset of the MIL-STD-883 standard for microelectronic devices, used widely by Military and Aerospace applications [4]. The MIL-STD-883 standard establishes uniform methods, controls, and procedures for testing microelectronic devices suitable for use within military and aerospace electronic systems. These procedures include extended testing to ensure the parts can withstand the environmental conditions (thermal and radiation) expected for the intended operating environment. Mechanical and electrical tests, workmanship and training procedures, and other such controls and constraints as deemed necessary to ensure a uniform level of quality and reliability are employed. Figure 3 shows JPL's tailored commercial microcircuit upsampling flow as implemented for Mars2020.

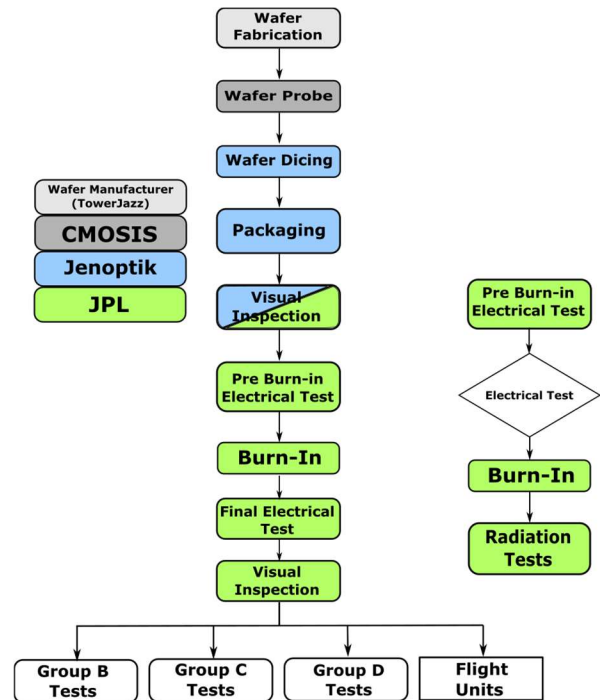


Figure 3. JPL tailored CMV20000 upsampling flow based on MIL-STD-883

Mars2020's investigation of the packaging and radiation performance of the CMV20000 detector proved the device suitable for OCO-3's thermal, vibration, and radiation environments. This work has enabled OCO-3 to infuse the highly capable, environmentally robust sensor into their Context Camera suite with minimal non-recurring engineering and low risk.

5. ELECTRONICS DESIGN

The OCO-3 Context Camera electronics design draws heavily upon initial work performed by the Mars2020 EECAM task. Camera electronics architecture, sensor interface design, and component selection were heavily leveraged to enable a rapid development for the OCO-3 project with minimal non-recurring engineering.

The design of the OCO-3 Context Camera electronics presented some challenges, including volume constraints presented by the project, sustainability of COTS parts, and a repeatable assembly and test procedure associated with miniaturization of the camera. Though the cameras are not mission-critical, there is a requirement that any potential failure mode shall not propagate across external interfaces to prevent damage to the OCO-3 instrument. Therefore, the camera's electrical design and choice of components abide by JPL's rigorous flight project derating and parts stress analysis criteria, providing enhanced reliability within an otherwise commercial camera system.

Electronics Topology

The Context Camera accepts +28V power from the spacecraft bus and delivers an image across the LVDS interface to the CEU up to every three seconds. To accomplish this, the camera includes power conditioning and distribution circuits, data processing and detector control within an FPGA, memory to store and buffer the image data, and LVDS transceivers to communicate with the host instrument.

The driving constraint for the electrical design of the Context Camera was to implement the required functionality of the camera within the allocated volume. The confined rectangular volume available to the cameras meant the electronics design needed to take advantage of all available space, and thus, the design grew in height rather than width. The electronics design was separated into multiple printed circuit boards, stacked one atop another, to maximize the camera footprint and still provide electrical connection between boards. This approach provided several advantages, such as isolating switching power regulation from the noise-sensitive detector, which allowed for reliable image quality and signal integrity due to noise suppression.

Figure 4 shows the electrical block diagram, as grouped into three printed circuit board designs, or 'slices'; Auxiliary board, Interface board, and Sensor board. Each slice uses a common mezzanine connector footprint to pass power and data signals between boards. This modular stackup allows for

future revisions of circuit boards to expand or augment camera capabilities.

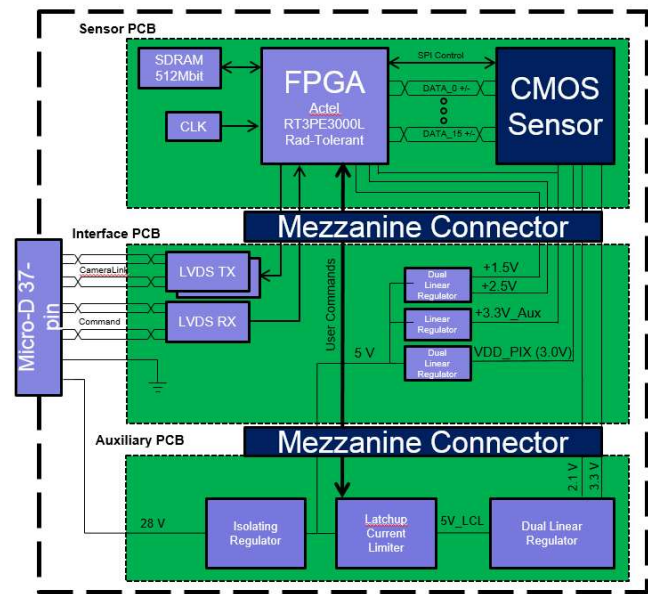


Figure 4. Context Camera electronics block diagram
(flight components in pink, COTS in dark blue)

The Auxiliary board resides in the bottom slot of the three-layer stack and houses a +28 to +5V DC/DC switching converter, a latch up current limiter (LCL), a dual output LDO voltage regulator, and some passive support components. The +5V output from the DC/DC converter is further regulated by the dual LDO to provide power supply rails dedicated to the detector. The LCL disables these power supply rails should it detect a current above a set threshold, due to latchup susceptibility of the CMOSIS detector. The +5V output passes up the stack to the interface board through the mezzanine connector.

The Interface board design serves as the middle slice, interfacing the Auxiliary board with the Sensor board, as well as the OCO-3 CEU and PCE. Two quad LVDS transmitters and one dual LVDS transmit/receive integrated circuits allow communication between the camera and the CEU. The Interface board also regulates power supply rails used for auxiliary power across the camera.

The Sensor board, the most complex and densely-populated slice, includes the CMOSIS detector, the FPGA, 512 Mbit SDRAM memory, a 120 MHz oscillator, and numerous passive support components. The FPGA serves as the controller for the entire camera, interfacing with the detector, memory, and components on both the Interface and Auxiliary boards.

The three boards are connected through fine-pitch surface mount high pin-count plastic mezzanine connectors. Power, data, and control signals are passed through these stacking connectors. Figure 5 shows a completed, assembled electronics stack for the OCO-3 Context Cameras.

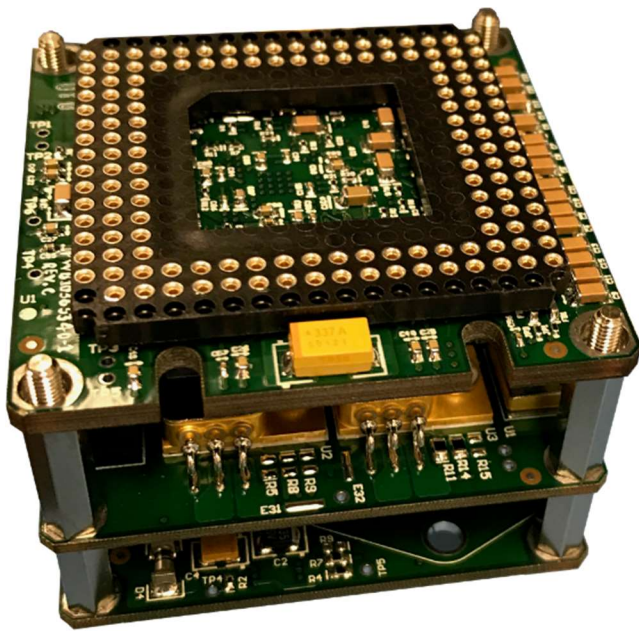


Figure 5. Context Camera electronics assembly (detector not shown)

Mitigation of Radiation Effects

The OCO-3 Context Camera design takes advantage of radiation-tolerant, MIL-STD-883 screened parts where possible. No additional reliability testing for these parts was performed, as these were classified as low-risk items for OCO-3's Low Earth Orbit on the ISS. The only two items that were not prequalified for space flight are the CMOSIS detector and the mezzanine connectors.

As previously mentioned, the detector has undergone extensive screening for radiation and thermal survivability at JPL. However, the detector was found to exhibit non-destructive latch up behavior in the presence of high-energy particles at approximately $30\text{MeV}\cdot\text{cm}^2/\text{mg}$, which was shown to disable functionality until the latch up is released by a power cycle of the susceptible power supply rails. The threshold for this behavior was below the expected radiation environment encountered in Low Earth Orbit. In order to preserve the detector's lifetime and maximize usage of the Context Camera, automated latch up current detection was implemented by use of a standalone latchup current limiter (LCL) circuit. Latchup current thresholds were defined empirically to define the repeatable detection and reporting of a latchup event.

Assembly and Test Complications

During camera electronics fabrication, issues related to surface mount assembly arose due to the miniaturization efforts implemented on the Sensor board. In order to maximize available electronics volume, the Sensor board uses a surface-mount ball grid array (BGA) socket to house the detector's 143-pin pin grid array (PGA) package. This allowed the detector to reside solely on the top side of the

board, leaving the other side for the FPGA, SDRAM, and support electronics. A side-view image of the Sensor board is shown in Figure 6.

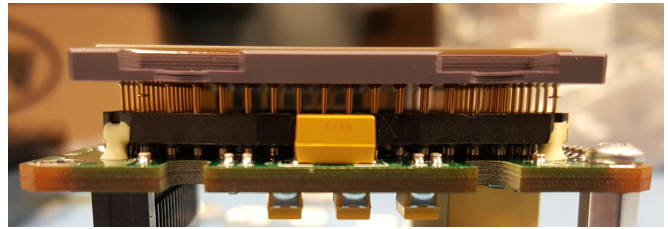


Figure 6. Side view of Sensor board, showing surface-mount BGA socket with detector

However, during the surface-mount assembly portion of the camera manufacturing process, multiple insufficient solder connections and open circuits were identified on the BGA socket. Due to the increased soldering complexity of the FPGA's package, the heavy BGA socket was creating difficulties when the PCB was reflowed on the bottom side for the FPGA. JPL's electronic packaging engineers developed a procedure using high-temperature, flight grade solder on the socket side of the PCB so that the solder joints would remain intact during installation of the FPGA. After multiple troubleshooting assembly runs, it was found that the socket side must be assembled first. Additionally, corner staking of the BGA and FPGA components helped the packages keep their orientation during the reflow process.

Risk of damage to the detector and electronics assembly related to the insertion of the detector into the BGA socket were also encountered. The nominal socket pins specified 75 grams per pin insertion force required to fully seat the detector. During functional testing of the prototype camera, anomalous behavior, such as varying impedance measurements and current draw based on physical orientation of the camera, led to the discovery of broken solder joints between the PCB and the BGA socket. These were found to be caused by the significant force required to mate the 143-pin detector to the socket. Switching from the 75 gram per pin socket to the lesser 25 gram per pin socket produced a repeatable detector assembly that did not risk damage to the flight hardware.

6. FPGA DESIGN

The interface between the instrument's data processing unit (DPU) and the camera's detector is handled by a custom firmware implemented in a radiation hardened FPGA. The purpose of this interface is to allow the DPU to command the acquisition of images with the desired parameters and to provide images in a format that can be directly interpreted by the receiving device. The FPGA functionality include four primary categories: interface with the detector control module, capture imaging data from the detector, buffer incoming frames into an SDRAM module and send out formatted frames to the data processing unit.

We used Synplify Pro for synthesis and Microsemi's Libero SoC for Place and Route. The final design uses 10.5% of the cells and 73.2% of the block-rams. The operating conditions were set to -30°C to +88°C with 8Krad of Total Radiation. The least slack reported under max conditions is 2.11ns on a 60Mhz clock domain. Figure 7 shows the FPGA block diagram.

configuration, some are expected to be set to a different value for each capture depending on the scene being looked at. The image brightness can be controlled by varying the exposure time or the gain of the analog signal chain inside the detector. Also selectable is the number of rows being read out for each frame.

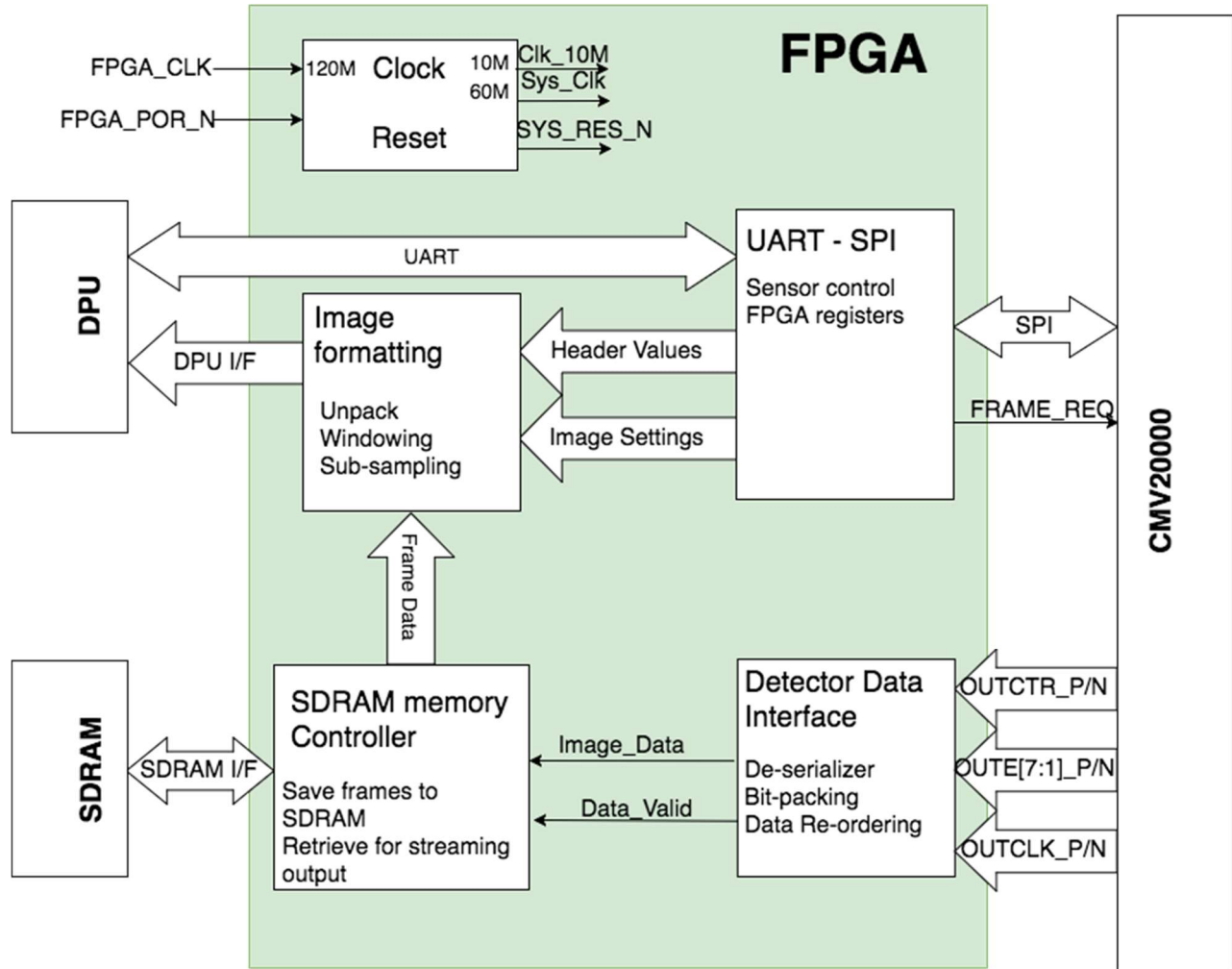


Figure 7. Camera FPGA block diagram

Command and Telemetry Interface

The DPU uses a universal asynchronous receiver-transmitter (UART) interface to send commands to the camera FPGA and to receive configuration information readback. Camera operating modes such as windowing and sub-sampling can be set via register settings through that communication channel. The detector itself communicates with a standard 4-wire serial peripheral interface (SPI) protocol for setting and reading back parameters. The FPGA translates the commands from UART to SPI to allow exercising the programmable options of the detector.

The operation of the camera is dependent on parameters that can be changed from their default values by accessing detector registers through this SPI interface. While most of those parameters are not to be modified for normal imaging

Image capture and formatting

The formatting of the images sent out from the FPGA is a function of the FPGA parameter values that are controlled with the UART interface. When retrieving frames from the SDRAM memory buffer, the "Image formatting" module converts the data from the memory allocation-efficient bit-packing format, detailed in the SDRAM implementation description, to an expanded format that can be directly interpreted by the DPU. This is done at the expense of bandwidth as every 12-bit pixel is then stored in a 16-bit format.

The "Image formatting" module also prepends to each image an 832-byte header containing information about the parameters of the image being transmitted. The content of the header is configured via UART-accessible registers.

The image output geometry can be modified in the FPGA to lower the image data size, hence the bandwidth necessary to transmit it. The camera implementation allows for two ways to achieve lower image size; windowing and sub-sampling. When the region of interest, defined by the user or the application, only covers part of the scene, the FPGA can complement the sensor's capability of reducing the vertical image size by reducing it in the horizontal direction. The windowed image has the same spatial resolution as the full image but only contains a fraction of the pixels. Sub-sampling also reduces data volume by skipping pixels in the image readout. Spatial resolution is reduced but the field of view is preserved.

Detector interface and image storage

The detector provides eight serial double data rate (DDR) data channels and one serial control channel synchronous to a 60Mhz Clock. The control channel provides a syncword that determines whether or not the data channels have valid data. The eight data channels increase the read-out speed of a 5120-pixel row by splitting it into 640 contiguous pixel segments. This makes it simple to crop the width of an image by ignoring data channels if desired. The detector also supports using sixteen data channels to further increase read-out speed by reading two rows in parallel, however bandwidth limitations between the detector and FPGA kept us from using this.

It is desirable to buffer an entire row of this data inside the FPGA so that the order of the row can be reconstructed from the data channels. This allows the data to be written to SDRAM in a linear fashion which leads to easier addressing and better bandwidth as the SDRAM controller isn't opening and closing rows as frequently in the SDRAM. Reconstructing the row before SDRAM also makes it easier to add data compression or error encoding in the future if desired. Two full row buffers are created with the FPGA block-ram so that we can operate the rows in a ping-pong fashion allowing one to be overwritten as the other is read for SDRAM.

Although the pixels coming from the detector are 12 bits, the SDRAM has a data-width of 16 bits and we are bandwidth limited by the SDRAM. Simply utilizing 12 of the 16 bits for SDRAM would not give sufficient bandwidth, making it necessary to break up the data in 16 bit segments where pixels are broken up. We decided to do this data regrouping immediately when the serial pixel data comes in since the data has to be deserialized regardless of whether it is to be formed into 12 or 16 bit segments. Doing the data regrouping here was also helpful because it leads to writing 16 bit segments instead of 12 bit pixels to row buffers which are created with FPGA block-rams that are 18 bits wide. Because of this we were able to use fewer block-rams to create the row buffers.

The design merely uses the SDRAM as a buffer to handle the bandwidth differential between the detector and the slower

camera interface. Though the image is sent over the camera interface in real-time the detector completes its read-out of the image in about 250ms but the camera interface takes about 3.5 seconds or longer. At ~24.6MB the buffering cannot be completed with FPGA block-ram.

Memory interface design trades

We utilized a commercially-available memory controller, CoreSDR v4.1 by Microsemi, in our design and used it to address the SDRAM as a large FIFO. The SDRAM controller could not be run at the 120Mhz clock speed provided to the FPGA due to timing limitations with Microsemi's ProASIC FPGA. The 120Mhz clock was divided to 60Mhz since we did not have a rad-hard phase-locked loop (PLL) available to generate other frequencies. Running at 60Mhz theoretically gives the bandwidth to store a full image that is 5120 pixels wide, but it does not allow for any overhead (or margin) in data writes. Margin is necessary however as bandwidth is lost when refreshing the SDRAM and also when opening/closing rows. To achieve the margin necessary, the image width was decreased from 5120 to 4480 pixels wide, effectively ignoring the last 640 columns of the image. The result was that only 87.5% of the detector pixels are captured and used for contextual imaging. This was an undesirable but necessary trade for both cameras, as the FPGA design could not keep up with the SDRAM timing requirements. Fortunately, the field of view and ground sampling distance requirements are still fulfilled with the reduction in image size.

7. MECHANICAL DESIGN

The camera's mechanical design supports the three electronics assemblies, detector, and optics. Figure 8 details an exploded view of the mechanical design and its components.

Opto-Mechanical considerations

In order to minimize focus drifts induced by thermal environments, the spacing of the detector to the lens interface had to be tightly controlled. This resulted in mounting the sensor to the same mechanical interface as the lens to ensure minimal errors in positional control (tip, tilt, and piston) of the detector within the focal plane of the lens. Focus adjustment to achieve proper lens to sensor spacing requires the use of a custom peel-able shim between the sensor chassis and the lens adapter.

Clamping the sensor package to this chassis had its own complications as we had to be careful to give proper pre-load to hold the sensor down for a good thermal path while not damaging the ceramic package of the sensor. Special clamps were designed to allow for these concerns.

The lens interface on sensor chassis included the ability to mount two very different types of lenses. Initially OCO-3 was able to use a common sensor chassis along with a lens

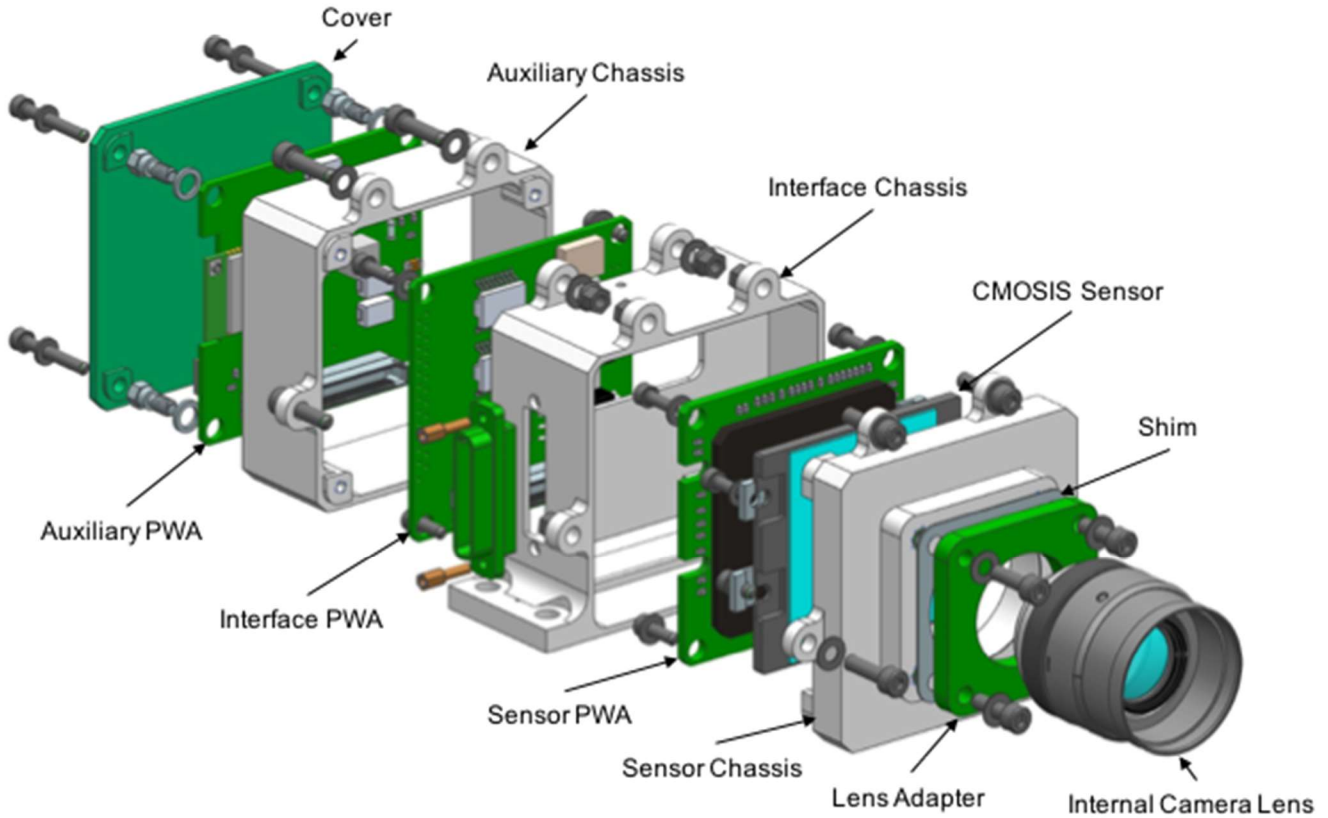


Figure 8. Exploded view of the Internal Context Camera

adapter, but due to space constraints at the lens location the sensor chassis for each camera was its own unique design. Future projects could most likely use the original sensor chassis with different lens types with a simple lens adapter change.

Electronics Packaging

Compared to the extreme thermal cycling of the Mars2020 EECAMs (-135°C to +70°C, 3000 cycles), robustness to large thermal excursions was not a concern for OCO-3, and a more aggressive miniaturization effort could be pursued. Strategic electronics packaging techniques and component selection enabled the camera to maintain robustness while fitting into the constrained volume allocation.

The camera uses a 143 pin Pin Grid Array (PGA) socket to attach the sensor detector to the Electronics. A prototype camera design had initially included a socket with a much greater pin insertion force and upon sensor installation caused stress on the board causing a component solder failure. An alternate PGA socket was attained and, although not an ideal mate between the sensor and the PGA socket, the forces used were not causing undue stresses to the board or its components. Board to board connections were achieved using plastic mezzanine connectors. This allowed for tighter spacing between boards, but meant tighter tolerancing was required on each chassis to make sure (the boards ended up with proper alignment and spacing to ensure) proper connector alignment and engagement.

8. CAMERA TESTING AND CALIBRATION

The cameras were tested to verify that all functional requirements were met, pre- and post-environmental testing. The tests performed on the camera include verification of command interface functionality, characterization of the detector (quantum efficiency, linearity, full-well, bad pixel identification, dark current), and imaging check after focusing of camera. Table 3 summarizes the ICC and ECC requirements against the capabilities of the cameras.

Table 3. Context Camera Requirements

Parameter	Requirement	Capability
ICC FOV	$\geq 4^\circ$	40.3° by design, limited by telescope aperture
ICC iFOV	≤ 0.22 mrad	0.22 mrad/pixel
ECC FOV	$\geq 25^\circ$	28.2°
ECC iFOV	≤ 0.5 mrad/pixel	0.125 mrad/pixel
Minimum SNR	$> 100:1$	$\leq 95:1^*$ * Performance accepted by project, limited by maximum achievable full-well of detector
Maximum Frame Rate	> 0.3 fps.	≤ 3.7 fps (ICC) ≤ 0.63 fps (ECC)
Date Rate	< 3 Mbps	1.77 Mbps

The ICC and ECC were found to meet all key and driving requirements, with the exceptions identified in the following discussion.

Focus Tests

Rough focus adjustments were performed using shim stock. Final focusing of each camera was carried out using a focus test for the ICC and a collimator for the ECC to adequately match the working distances for each lens. The target was imaged repeatedly and lens shimmed until best focus achieved. Figure 9 shows a cropped, vignetted image at best focus position for the ICC. Figure 10 shows a cropped image at best focus for the ECC.



Figure 9. Cropped ICC image after fine focus adjustment (975 x 810 pixels)



Figure 10. Cropped ECC color image after fine focus adjustment (638 x 745 pixels)

Field of View and iFOV measurements

Field of view and angular sampling, or instantaneous Field of View (iFOV), measurements were performed by imaging a focus target of known dimensions at a known distance for each camera. Using a focus target at known distance, the angular size of the target was calculated and number of pixels across the focus target measured from image data, using Equation (1). Figure 11 shows the ICC and ECC focus targets, as imaged by their respective camera. Note the ‘checkerboard’ bayer pattern is visible in the ECC raw image output, as use of the raw monochromatic image avoids interpolation effects introduced after the ‘debayering’ algorithm in software to produce a color image.

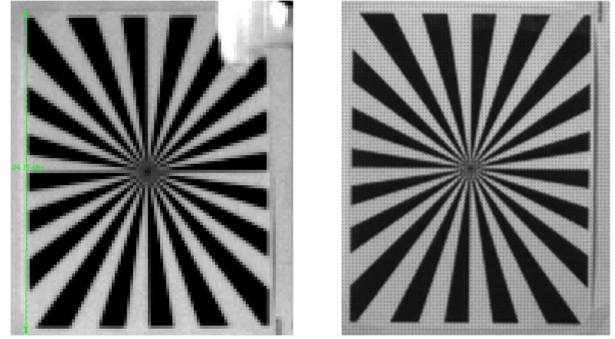


Figure 11. ICC (left) and ECC (right) focus target images at 12.1m.

$$iFOV_{radians} = \frac{\arctan\left(\frac{2*f}{d}\right)}{\# \text{ of pixels}} \quad (1)$$

Where f = the camera’s focal length in millimeters, d = distance of the object in meters, and $\# \text{ of pixels}$ is the count of pixels subtending the target.

$$iFOV_{ICC} = 0.22 \text{ mrad/pixel}$$

$$iFOV_{ECC} = 0.125 \text{ mrad/pixel}$$

Both the ICC and ECC were shown to meet the angular sampling (iFOV) requirements.

The pixel geometry of a context camera image is 4480 x 3839 pixels. Using the measured iFOV, the field of view of each lens is calculated and converted to degrees with Equations (2) and (3) respectively:

$$FOV_{rad} = (Pixels_{Horizontal} \times Pixels_{Vertical}) * iFOV \quad (2)$$

$$Degrees = Radians * \frac{180}{\pi} \quad (3)$$

$$FOV_{ICC} = 986 \times 845 \text{ mrad} = 56.5^\circ \times 48.4^\circ$$

The ICC requirement is a FOV of $\geq 4^\circ$.

$$FOV_{ECC} = 561 \times 492 \text{ mrad} = 32.1^\circ \times 28.2^\circ$$

The ECC meets its FOV requirement of $\geq 25^\circ$.

Frame Size and Frame Rate

The frame size requirement for each camera dictates the need for a sufficient number of pixels in every image to meet the minimum Field of View.

Though the ICC FOV far exceeds the requirement of $\geq 4^\circ$, the ICC must window the sensor to meet the framerate requirement. Therefore, the ICC outputs a programmable window size, nominally set at 400 x 400 pixels, providing a $5.03^\circ \times 5.03^\circ$ FOV.

A minimum ECC frame size of 3490 x 3490 is necessary to meet the Field of View requirement of $\geq 25^\circ$. However, the resultant frame rate does not meet the requirement of 0.3 frames per second. The project chose to waive this requirement, and would operationally change the desired frame size and sub-sampling factor to balance frame rate, given the calibration scenario.

The maximum frame rate of a camera is calculated by measuring the time taken for 10 consecutive readouts of a detector sub-region at minimum exposure time.

The measured maximum rate of the ICC at 400 x 400 pixels was 3.7fps. The measured maximum frame rate of the ECC is summarized in Table 4, where selectable frame size and sub-sampling are used to achieve a desired frame rate. With a sub-sampling factor of 2x2, the iFOV increases by a factor of two, but still meets the minimum ECC iFOV requirement.

Table 4. ECC Frame Rate parameters

Frame Size (pixels)	Sub-sampling factor	Frames per Second	FoV (degrees)	iFOV (mrad/pixel)
4480 x 3839	None	0.1	32.1 x 28.2	0.125
3490 x 3490	None	0.2	25 x 25	0.125
2656 x 2656	None	0.5	19 x 19	0.125
1328 x 1328	2x2	0.63	19 x 19	0.25

Detector Characterization Testing

Imaging performance of the Context Cameras relies on the rated performance of the CMV20000 detector. Detector linearity, full-well capacity, dark current, quantum efficiency (QE), bad pixel identification, and pixel response non-uniformity (PRNU) were measured. All tests were performed at 21°C.

The photon transfer curve (PTC) is a very important diagnostic tool for determining the performance of a detector. A series of pairs of frames with increasing exposure times are acquired. For each pair of frames a number of samples of the mean and variance of the sum and difference of the two frames is computed. The individual samples are taken as a

small box of pixels within the image frame (typically a few tens of pixels on each side). A plot of the mean versus square-root of the variance is plotted. The plot can be used to determine the read noise floor, linearity, conversion gain (e-/DN) and full well of the detector.

The CMV20000 has two gain stages in the video chain – a pre-ADC amplification stage (PGA) and gain in the ADC sampling process. Each can be adjusted to match the full-well of the sensor to the 12-bit ADC resolution. Figures 12 and 13 show PTC curves for two (2x) PGA gain settings and for two (2x) different ADC gain settings. The purpose was to identify the optimum gain settings. Table 5 summarizes the final parameter settings.

The illumination was a tungsten lamp with brightness adjusted to saturate the detector in approximately 8ms – matching the maximum OCO-3 exposure time.

Table 5. Photon Transfer Curve parameters

Camera	ADC Gain	PGA Gain	Conversion Gain (e-/DN)	Full Well (e-)	Full well (DN)	ADC Saturated (4095DN)
ICC	57	1x	3.4	13000	3800	Close
ECC	57	1x	3.5	12800	3650	No

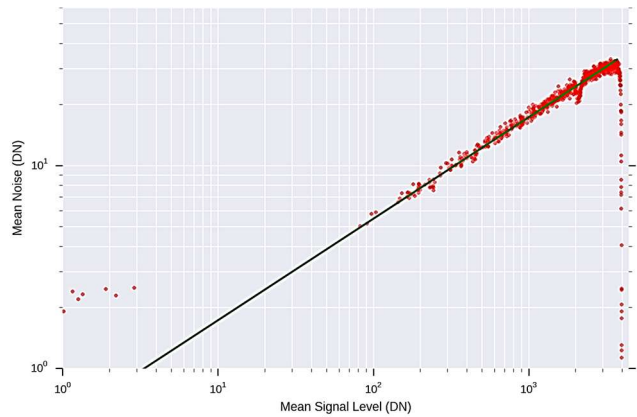


Figure 12. Photon Transfer Curve for ICC

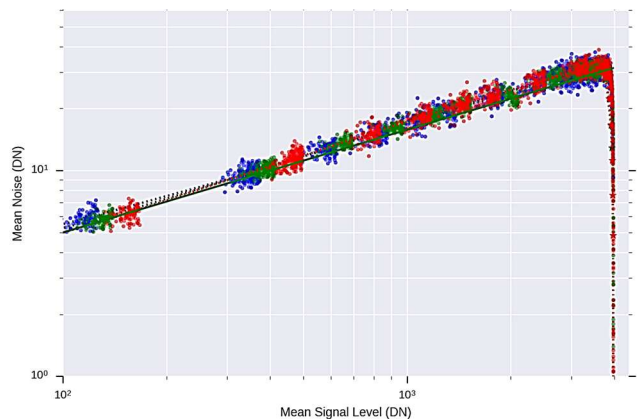


Figure 13. Photon Transfer Curve for ECC

The PTC curves show a sensor which behaves linearly over its dynamic range. For many of the gain settings the ADC saturates before the pixel reaches full-well. The full well measurement is accurate to a 200-300 DN. The conversion gain measurements align well with the rated datasheet values.

Signal to Noise Calculation – The full-well measurements allow the maximum SNR achievable in a single image to be calculated. The SNR requirement is for SNR > 100 at 70% full-well. The theoretical maximum SNR can be found with Equation 4:

$$SNR_{Max} = \sqrt{Signal_{e-}} \quad (4)$$

Using the values at optimal gain settings per Table 4:

$$SNR_{Max} = \sqrt{(0.7 * 13000)} = 95$$

Though the camera performance does not meet the SNR requirement of ≥ 100 , the project deemed the camera capability acceptable.

Dark Current – Dark current is due to thermally generated charge carriers entering the pixel or sampling circuitry. Dark current measurements were performed by taking a series of dark exposures at increasing exposure times and plotting the measured dark signal average over a sub-region 400 x 400 pixels within each image. A plot of mean pixel value within a sub-region was calculated at each exposure time and a 1st order polynomial function fitted. The gradient of the line was calculated to be 284 e-/s.

Measurements were taken after camera was left on for several days and ambient temperature was 24°C. Camera was warm to touch and internal detector temperature would be somewhat higher than 24°C.

The datasheet value for the detector dark current rate is 125e/s. Using the empirical relation for silicon that dark current increases by a factor of 2x for each 6.5°C increase in temperature, the numbers would be consistent with the detector was 7.7°C warmer than ambient. This is plausible and consistent with data.

Read Noise – Read noise is the irreducible limiting noise in a detector system. Read noise was measured from two minimum exposure time frames. Frames are subtracted from each other and then the pixels sorted and the top and bottom 10% discarded. The noise statistics of the remaining pixels were then used to calculate the read noise, summarized in Table 6.

Table 6. Detector read noise measurements

Camera	Read Noise (e-)
ICC	11.3
ECC	8.1

The read noise for the ECC matched closely with the reported datasheet value, but the ICC measurement was higher than expected. The source of this mismatch is unknown, but likely due to device-to-device variance.

Linearity – The linearity of the detector response to increasing illumination was performed. A series of successive exposures of different exposure times were acquired and the mean value within a sub-region in each image determined. This was plotted against exposure time and a straight-line fit performed, as shown in Figure 14. A second plot showing the ratio of the difference between the data and the model scaled by the data was made. The device gain settings were set to the parameters in Table 5. Non-linearity is to within ~1% across the signal range of the detector.

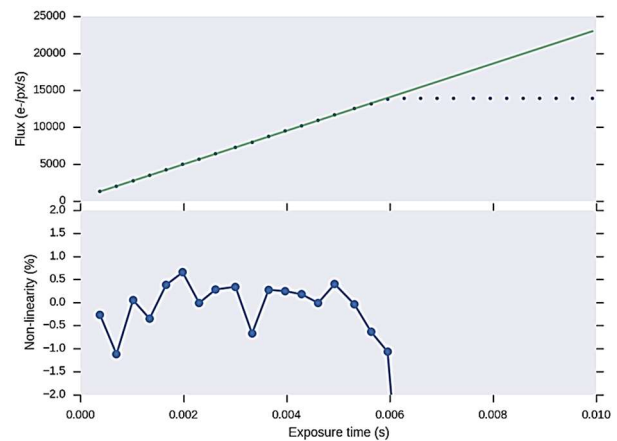


Figure 14. Detector linearity plot

Quantum Efficiency - Quantum efficiency (QE) is measured by determining the response of the detector to illumination at specified wavelengths. The testing apparatus consists of a broadband light source, which is fed into a monochromator. The grating internal to the monochromator is tuned to select a specific wavelength of light, which passes through the instrument exit slit. The width of the slit determines the absolute spectral width of the line, and can be adjusted to provide a trade-off between wavelength precision and sufficient flux for high-SNR measurements.

The monochromatic light leaving the monochromator exit slit falls directly onto the camera. A separate calibrated photodiode is used to measure the slit flux. The relative fluxes at the photodiode and detector are measured and the QE of the detector determined. Figures 15 and 16 show the measured QE for the ICC and ECC respectively.

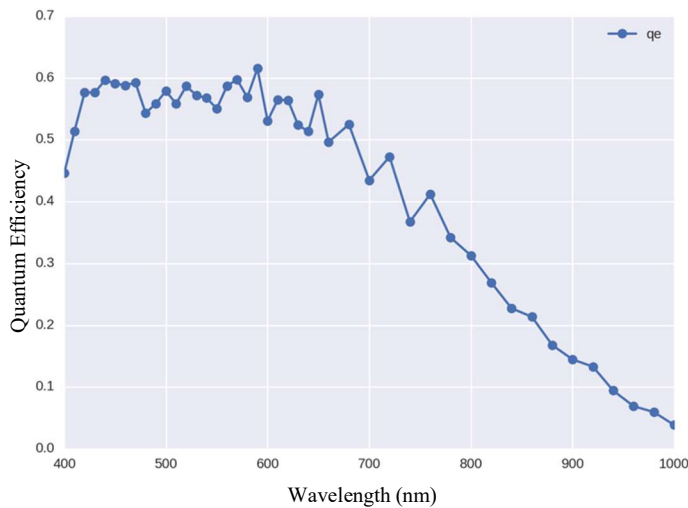


Figure 15. QE curve for ICC at 294k

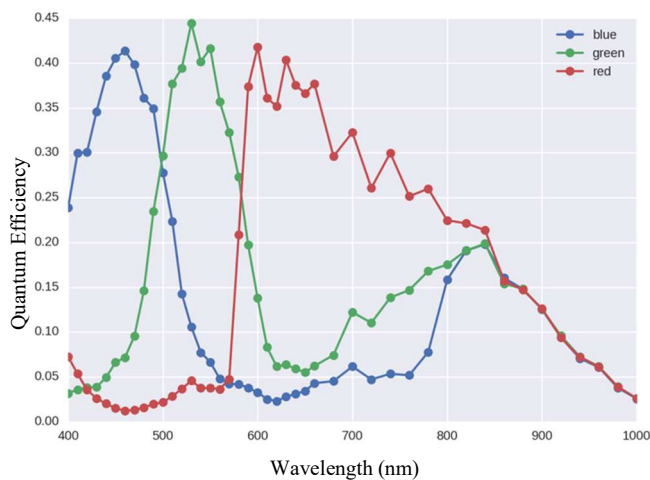


Figure 16. QE curve for ECC at 294k

The measured curves are in good agreement with the expected curves from the detector datasheet, although the fall-off below 500nm is not as quick in the measured data as in the datasheet predictions.

Pixel Response Non-Uniformity – The pixel response non-uniformity (PRNU) is a measure of the variation in the pixel sensitivity across the device. The PRNU was calculated by combining multiple flat field images and then evaluating the standard deviation, divided by the mean value, of the pixel values over a sub-region of the chip. Figure 17 shows stacked and averaged flat fields of the ICC illuminated with 640nm light. This same process was also performed for the ECC PRNU measurement.

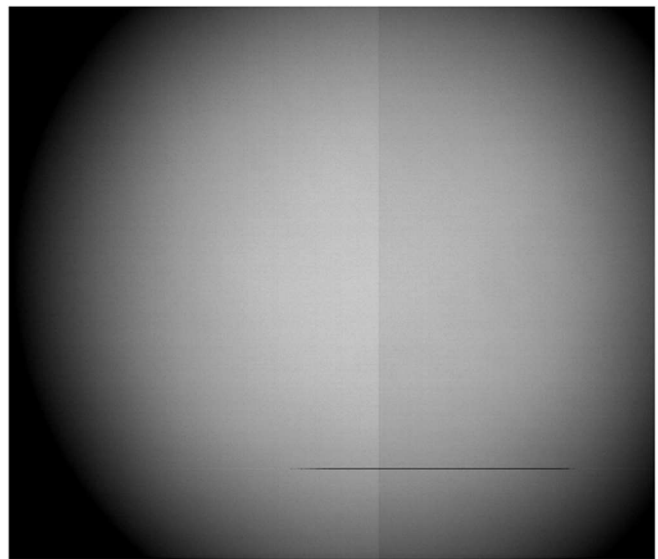


Figure 17. Ten ICC average flat fields illuminated with broadband light at roughly full-well illumination

An average dark frame of identical exposure time has been subtracted. The gain difference between the left and right half of the chip are clearly evident. Averaging across ~100 rows within ~20 columns of the transition the gain ratio is measured as ~2.7%. This could equally well have been determined from measuring the conversion gain with PTC analysis on the left and right hand side of the detector (all PTC curves were generated using only the left-hand-side of the detector). This gain difference is eliminated by normalizing or flat-field images once SNR becomes sufficiently high to see the step across the sensor, as seen in Figure 18. Note the left and right hand side transition is not in the middle of the device as one right-hand channel of image data (640 pixels) is not included in the delivered camera images.

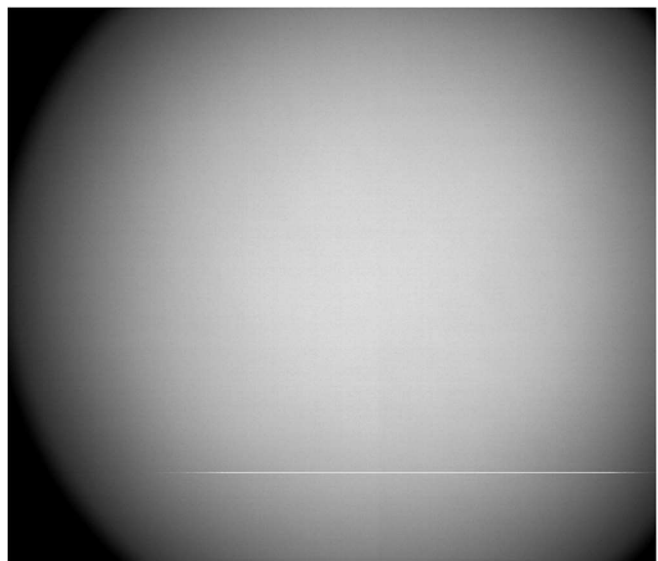


Figure 18. ICC flat field image post-PRNU correction

Final Integration

The ICC and ECC were delivered to the OCO-3 Integration and Test operations in April 2017 and were successfully integrated within the instrument. Figure 19 shows the completed ICC during optical testing. Figure 20 shows the ICC integrated onto the instrument's telescope.

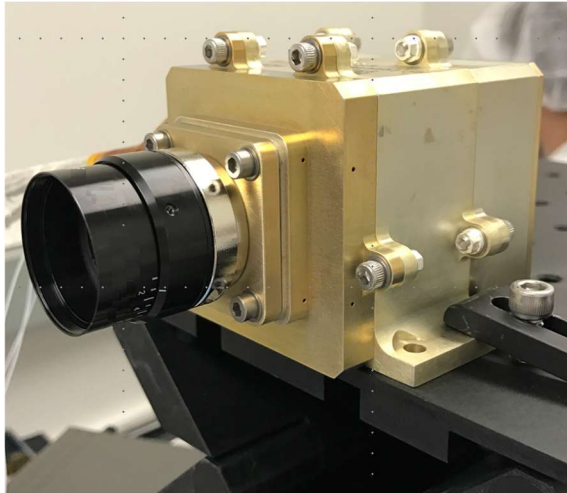


Figure 19. Completed Internal Context Camera

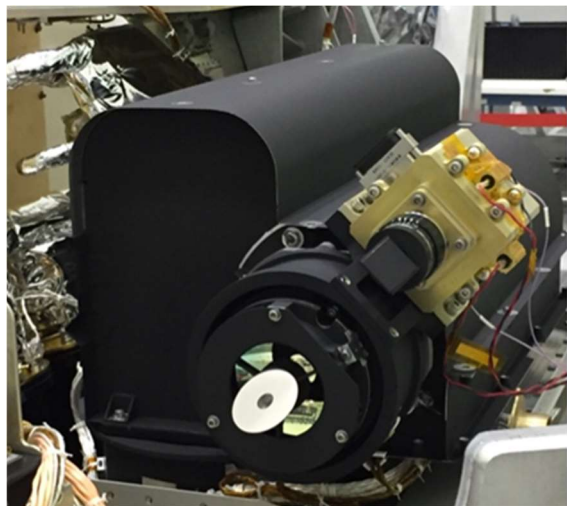


Figure 20. ICC integrated with the OCO-3 entrance optics

Environmental Testing

The Context Cameras were subjected to limited environmental tests at the subsystem (camera) level prior to delivery to OCO-3 Integration and Test. Limited testing included only the aforementioned Thermal Vacuum (TVAC) and Vibration tests on the COTS lenses, and electro-magnetic interference and conductance (EMI/EMC) testing performed at the camera level.

System-level TVAC, vibration, and pyro-shock testing were performed following integration of the ECC and the ICC to

their respective next levels of assembly.

Both cameras successfully completed TVAC thermal cycles, passing functional tests while operating from -20°C to +60°C.

The ICC underwent Flight Acceptance random vibration testing following its integration with the instrument's entrance optics. This testing enveloped the loads expected for the ECC on the PMA, which saw lower levels when tested at its next level of assembly. Table 7 summarizes the vibration environments subjected to the ICC at the next level of assembly.

Table 7. ICC and ECC Vibration levels

Test Article	Frequency (Hz)	Flight Acceptance Levels	Qualification/Protoflight Levels
Internal/External Context Cameras, Entrance Optics	20	0.008 g ² /Hz	0.016 g ² /Hz
	20-50	+ 6 dB/octave	+ 6 dB/octave
	50-300	0.05 g ² /Hz	0.10 g ² /Hz
	300-2000	- 6 dB/octave	- 6 dB/octave
	2000	0.0011 g ² /Hz	0.0023 g ² /Hz
	Overall	5.1 grms	7.2 grms

Pyro-shock levels for the ICC are expected to be very low for the OCO-3 instrument (excluding PMA) due to the instrument's isolation system and did not require test verification. However, the PMA (including the ECC) is subject to near field pyro-shock due to a 3/8" frangibolt separation event while docking with the International Space Station. Therefore, the PMA (with ECC) was tested to the levels shown in Table 8.

Table 8. PMA with ECC Pyro-shock levels

Test Article	Frequency (Hz)	Maximum Shock input to payload (g-peak SRS)	Maximum Shock input to payload +3 dB (g-peak SRS)
External Context Cameras, PMA	100	52	73
	1300	3000	4200
	10,000	3000	4200

9. POTENTIAL FOR FUTURE USE

The OCO-3 Context Camera architecture has the potential to be infused in future NASA/JPL missions, either as a build-to-print solution or adapted per specific mission requirements. Data and power interfaces, image processing within the FPGA, mechanical form-factor, and optical performance can be tailored with minimal non-recurring engineering.

One such instance of low-cost infusion is the NEAScout Cubesat mission to investigate near-earth asteroids [5]. Due to an extremely limited budget and schedule, the OCO-3 Context Camera was baselined as both the instrument's star-tracker and its science camera. A new mechanical chassis was designed to house the build-to-print electronics assemblies,

and an alternate COTS lens was procured to meet mission imaging requirements. Finally, the existing FPGA design was modified to support the Spacewire data protocol without any changes to the electronics hardware. The result is a high-heritage camera system successfully delivered within a heavily-constrained Cubesat budget and schedule.

Another application for the Context Camera is for planetary missions involving landers or rovers where visual odometry, or image-based motion tracking, is used during the spacecraft's entry, descent, and landing (EDL) phase. As is the case with NASA's Mars2020 mission, a camera is used to supplement the landing radar system to provide image-based position and motion tracking for the spacecraft during EDL. The spacecraft compares real-time imagery of the Martian surface with known ground-truth maps to provide fine closed-loop control of the EDL sequence, effectively minimizing the spacecraft's landing ellipse error. Tighter control of the landing of the spacecraft enables a greater potential for science return in feature-rich areas previously deemed too risky to land due to neighboring hazards.

Finally, the Context Cameras could be deployed as a monocular or stereoscopic tracking system for spacecraft attempting to rendezvous with other spacecraft, such as docking operations or small payload retrievals. The windowing and binning capability of the cameras allow scalable machine vision stereo ranging performance and centroiding accuracy at various object distances at the expense of frame rate, and could provide a drop-in solution for future missions to add this capability. The Mars Sample Return concept is one example, where the sample return payload will require precision rendezvous with the return spacecraft while orbiting Mars.

10. SUMMARY

Two visible-band contextual imaging cameras, the Internal Context Camera and External Context Camera, were successfully designed, built, and tested at JPL and delivered to the OCO-3 project. Significant non-recurring engineering was leveraged from Mars2020 Enhanced Engineering Cameras to enable rapid development on a cost- and schedule-constrained effort. The wide range of applications for these cameras and their modularity allow low-cost infusion of tailored visible imaging systems in future NASA missions.

ACKNOWLEDGEMENTS

The authors thank Matthew Bennett, Said Kaki, Randy Raasch, Misrahim Morales, Thomas Werne, Matthew Ryan, and Marian Stokes for their contributions to the successful design, test, and delivery of the OCO-3 Context Cameras.

The work described in this paper was carried out at the Jet Propulsion Laboratory, California Institute of Technology, under a contract with the National Aeronautics and Space Administration.

REFERENCES

- [1] NASA/JPL. "OCO-3 Mission Summary." oco3.jpl.nasa.gov, NASA/JPL, 2017. Web.
- [2] CMOSIS. "CMV20000 datasheet v2.3" cmosis.com, AMS Sensors Belgium, 2015. Web.
- [3] Maki, J. N., et al., Mars Exploration Rover Engineering Cameras, J. Geophys. Res., 108(E12), 8071, doi:10.1029/2003JE002077, 2003.
- [4] *Test Method Standard, Microcircuits*, MIL-STD-883K, 2017
- [5] NASA. "NEAScout Mission." nasa.gov/content/nea-scout, NASA/JPL, 2017. Web.

BIOGRAPHY



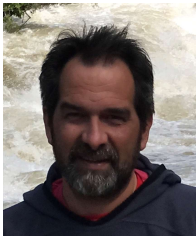
Colin McKinney received his B.S. degree in Electrical Engineering from Cal Poly, San Luis Obispo in 2008. He is a member of the Flight Detector and Camera Systems group at JPL, responsible for the delivery of the Enhanced Engineering Cameras for the Mars2020 Rover. He is also active in the research and development of the enabling technologies for extreme environment (wide-temperature, high radiation) visible camera systems for NASA's planetary missions to Mars and the Jovian system.



Dr. Timothy Goodsall received his DPhil in Astrophysics, specializing in instrumentation, from the University of Oxford in 2009. He is a Technologist within the Advanced Detectors, Systems and Nanoscience group at JPL specializing in the development and characterization of detectors and instrument systems.



Dr. Michael Hoenk earned a Ph.D. in Physics from the California Institute of Technology in 1990 for research on spontaneous nanometer-scale segregation and ordering in MBE growth of III-V semiconductors on non-planar surfaces. He is a member of the Nano and Micro Systems group at JPL, with 20 years' experience in advanced sensor development and instrument integration for NASA applications in Earth and Space Science.



Doug Moore is a mechanical engineer specializing in optical and imaging systems at NASA's Jet Propulsion Laboratory.



Dr. Muthu Jeganathan received his B.S.E.E. from USC and his M.S. and PhD in Electrical Engineering from Stanford University. He is the Instrument Manager for the OCO-3 project and a member of the Instrument Systems Implementation and Concepts section at NASA's Jet Propulsion Laboratory.



Dr. Christophe Basset is an Instrument System Engineer in the Flight Instrument Detectors and Camera Systems group at JPL. After receiving his Ph.D. in 2007 from the California Institute of Technology while researching at JPL, he worked on custom cmos image sensors in the private sector. His interests included

focal-plane image processing, internal timing controls for different types of pixel and readout architectures, mixed-signal circuits, high-speed interfaces and image sensors in general. At JPL, where he returned in 2016, he is involved in the support and development of various instrument and imaging systems, including for the Mars2020 rover and NEAScout Cubesat.



Jacob Shelton graduated with his B.S. and M.S. degrees in Electrical Engineering from the University of Tennessee, Knoxville, in 2013 and 2015, respectively. He is an Electronics Engineer in the Instrument Electronics group at JPL, which specializes in the design of application specific space-grade electronics to support and interface

science detectors to ground data systems for flight instruments. While at JPL, he has delivered flight electronics for both the OCO-3 and ECOSTRESS instruments, and presently is responsible for the development and delivery of the Camera Electronics system for the Multi-Angle Imager for Aerosols (MAIA) mission.



Keith Rumney received his B.S. and M.S. degree in Electrical Engineering from UCLA in 2015 and 2016, respectively. He is an Electronics Engineer in the Flight Instrument Detectors and Camera Systems group at JPL. He is involved in the FPGA design and verification of various imaging systems including for the

NEAScout cubesat, the Multi-Angle Imager for Aerosols (MAIA), and the Mars2020 rover.